Design and performance analysis of a highly sensitive photonic crystal fiber based plasmonic sensor

Abdullah Walid[1] · Tonmoy Roy[1] · Md. Mehedi Hasan[1] · Mahfujur Rahman[1] · Md. Kamal Hossain[1]

Abstract

This article presents a highly sensitive plasmonic sensor with a focus on enhancing its capabilities through innovative design and simple geometric structure. A hexagonal-shaped photonic crystal fiber (PCF) based surface plasmon resonance sensor is designed and proposed for external sensing applications. The plasmonic material is made of gold and positioned on the outer side of the designed PCF. For detection purposes, the flow of the testing analyte is introduced on the exterior section of the PCF. The sensing capability of this innovative sensor is meticulously examined using the finite element technique facilitated by the COMSOL Multiphysics software. The suggested sensor, with a refractive index of 1.38, has a maximum amplitude sensitivity and wavelength sensitivity of 765.86 RIU^{-1} and 8,000 nm/RIU respectively. At the same refractive index, the sensing resolution of the sensor is 1.31×10^{-5} for amplitude sensitivity and 1.25×10^{-5} for wavelength sensitivity. Additionally, the sensing capability of the sensor lies in the range of the analyte refractive indices from 1.33 to 1.39. Furthermore, the sensing performance of the designed sensor is analyzed by optimizing the values of several design parameters including air-hole diameter, pitch, and gold layer thickness. The suggested sensor can recognize biological analytes with high sensitivity, improved sensing resolution, and appropriate linearity.

Keywords Surface plasmon resonance (SPR) · Photonic crystal fiber (PCF) · Plasmonic biosensor · External sensing · Highly sensitive

1 Introduction

Surface plasmon resonance (SPR) is a fascinating optical detection technique because of its extremely sensitive performance (Momota and Hasan 2018). Due to its wide range of applications in biological analyte detection, chemical detection, medical diagnostics, and environment monitoring during the past few decades, SPR is quite well-known (Liu et al. 2023). Kretschmann SPR sensors have become increasingly popular because of their

✉ Mahfujur Rahman
 mahfujurrahmanruice@gmail.com

[1] Department of Electronics and Communication Engineering, Hajee Mohammad Danesh Science and Technology University, Dinajpur-5200, Bangladesh

excellent sensing capabilities. However, these sensors are limited by their huge size and the presence of moving mechanical parts, which hinder miniaturization and enhancement. To address these limitations, PCF sensors have appeared as a favorable alternative (Gangwar and Singh 2017). PCFs have also become a promising substitute for prisms for sensing applications in the recent few years. It offers numerous advantages over conventional prisms, including their compact size, simpler light coupling mechanisms, propagation in only one mode, and the ability to control the penetration of evanescent fields. These advantages have made PCFs an attractive candidate for SPR sensor development. The miniaturized size of the PCF sensors is particularly advantageous, and their sensitivity can be further enhanced by optimizing design parameters for instance pitch distance, number of rings, and air-hole dimensions (Hasanet 2018).

SPR occurs at the interface between a metal and a dielectric material, such as the core and surrounding medium of a PCF. This phenomenon arises from the simultaneous movement of electrons, known as surface plasmon waves (SPWs), induced by the interaction of incident light with the metal surface. The resonance condition occurs when the energy and velocity of the incident light match those of the SPW, resulting in a sharp increase in the reflected intensity, which is exploited in SPR-based sensing mechanisms (Rifatet. 2017). The propagation of the surface plasmon wave at the metal/dielectric interface is very sensitive to variations in the refractive index of the surrounding medium (analyte) of the PCF. This property enhances the PCF sensors' sensing abilities (Otupiri et al. 2015). The air holes in PCFs allow for tighter confinement of light in the core compared to traditional fibers. This stronger confinement leads to a more intense interaction between the light and the surface plasmons on the metal coating, resulting in a sharper and more sensitive SPR signal (Miyazaki et al. 2017). By adjusting the diameter and arrangement of air holes in the PCF core, the researchers can tailor the confinement properties of the core mode. A tighter confinement (smaller air holes) leads to a stronger interaction between the evanescent field of the core mode and the SPPs on the metal coating, enhancing coupling efficiency (Jing et al. 2022).

Surface plasmon resonance (SPR) is typically induced by gold, silver, copper, or aluminum in PCF-based sensors. Among these materials, silver exhibits exceptional performance since it doesn't have an interband shift and low dissipation of energy. However, its sensitivity is hampered by the formation of a fragile oxide layer in aqueous environments (Smith et al. 2024). Aluminum, another promising plasmonic material, also suffers from oxidation issues despite its high electron density. In contrast, gold stands out as an organic-friendly metal with excellent chemical stability in aqueous environments. Additionally, it offers a large resonance peak shift and is relatively easy to fabricate (Rifat et al. 2017). PCF-based sensors are typically divided into two categories: sensors with internal metal coating and sensors with external metal coating. Both kinds include inserting the metal and liquid analyte into designated air holes located in the inner section of the PCF. In sensors with an internal metal coating, the air holes are filled with the deposited plasmonic material, while in sensors with an external metal coating, the coating is used on the external surface of the PCF. Despite offering high sensitivity, internal metal-coated sensors pose a challenge in terms of accurate deposition of the material with plasmonic properties in the designated area of the PCF. On the other hand, external metal-coated sensors have the benefit of maintaining high sensitivity while simplifying manufacture by keeping both the analyte and the plasmonic material outside the PCF surface (Chen et al. 2024; Jabir and Areebi 2022). PCF-based SPR sensors offer exciting possibilities, but they also come with some limitations. Complex and expensive fabrication hinders mass production, and traditional material data

might not perfectly translate to PCFs, affecting analyte detection accuracy. Additionally, optimizing light-plasmon interaction adds development complexity. Overcoming these limitations through fabrication advancements, improved material modeling, design optimization, and regeneration techniques will unlock the true potential of PCF-based SPR sensors.

In recent times, due to numerous advantageous features, researchers have focused their attention on designing and developing PCF-based SPR sensors. Ahmmed A. Rifat et al. (2017) present a noteworthy contribution to the development of biosensors, introducing a PCF biosensor with surface plasmon resonance. Employing a basic hexagonal lattice configuration, the biosensor, coated with chemically stable gold, demonstrates high sensitivity and resolution. With maximal sensitivities of 4000 nm/RIU and 478 RIU^{-1}, this design operates within the interval of 1.33–1.37. Sharmin et al. (2018) present a significant contribution in their paper. The innovative design showcases a circular PCF sensor, minimally affected by structural parameter variations, and demonstrates robust sensing accuracy, reducing machining errors. Employing finite element analysis, the biosensor achieves remarkable performance featuring a maximum wavelength sensitivity reaching 8000 nm/RIU, a mean wavelength sensitivity reaching 3142.9 nm/RIU, and an amplitude sensitivity of 80.29 RIU^{-1} within the 1.33–1.38 refractive index range. Hossain et al. (2019) introduce an innovative biosensor with high sensitivity. Utilizing the material with the plasmonic properties being gold and incorporating an outer sensing medium, the structure proves effective for detecting biomolecular analytes. This sensor attains remarkable performance, showcasing a maximum sensitivity of 4000 nm/RIU and a resolution of 2.5×10^{-5} RIU. Seifouri et al. (2018) present a cutting-edge biosensor. Employing gold as the material with plasmonic properties, the sensor's inventive configuration positions metal and sensing layers beyond the fiber structure, simplifying fabrication and analysis. Utilizing the numerical method using finite elements, the biosensor achieves a remarkable maximum sensitivity of 5723.5 nm/RIU and a resolution of 1.74×10^{-5} RIU through wavelength interrogation. Rifat et al. (2016) propose an innovative biosensing approach. By positioning the plasmonic metal and sensing layers external to the fiber structure, the sensor configuration is streamlined. Utilizing copper as a material with plasmonic properties, with graphene preventing oxidation, the biosensor exhibits notable stability. Numerical analyses reveal a remarkable average wavelength sensitivity of 2000 nm/RIU and a resolution of 5×10^{-5} RIU. An et al.'s (An et al. 2017) unveil a pioneering quasi-D-shaped PCF for near-infrared refractive index sensing. With a wavelength interrogation sensitivity spanning 3908–10,693 nm/RIU and a peak amplitude sensitivity of 95 RIU^{-1} at 2040 nm, this design surpasses traditional D-shaped fibers, offering simplicity in fabrication. Ng et al. (2018) introduce a groundbreaking diamond ring fiber design with a gold-coated cavity, offering direct analyte infiltration. Numerical analyses reveal impressive wavelength and amplitude sensitivities 6000 nm/RIU and 508 RIU^{-1} respectively across a refractive index range of 1.33–1.39.

This paper proposes a novel biosensor design with a simple modified hexagonal lattice structure. The sensor features two hexagonal ring-shaped air holes. The external surface houses both the sensing medium and the gold layer. This configuration avoids coating the inner air holes, simplifying fabrication. The choice of gold as the plasmonic material is driven by its chemical stability when exposed to aqueous environments and its ability to generate strong resonance peaks. Furthermore, we tuned the structural parameters to investigate their influence on the sensor's performance and ultimately identified the configuration that maximized sensitivity.

2 Sensor design and theoretical modeling

Figure 1 presents a cross-sectional view of our modified hexagonal PCF featuring two hexagonal rings. The pitch distance (Λ) of two adjacent air holes is set at a constant value of 2 μm. The diameter of smaller and larger air holes is d1 = 0.3 × Λ and d2 = 0.65 × Λ. The absence of two specific air holes-one centrally and two vertically in the second ring facilitates enhanced field contact with the sensing layer. As a result, the metal-dielectric surface allows surface plasmons to propagate through it effectively and efficiently.

The suggested design structure is built using fused silica, and the air holes are intentionally left vacant. A gold layer of 40 nm thickness is applied to the outer surface (t_g). The Drude-Lorentz model describes the dielectric constant of gold. The analyte layer, positioned above the gold layer, serves as a sensitive detector for the target analyte, and the most external layer is composed of the Perfectly Matched Layer (PML). To ensure highly accurate simulations, we employed a physics-controlled mesh with finer element size. The widths of the PML and analyte layer are set at 1.2 and 1 μm respectively.

We select the appropriate substance that affects the suggested sensor's sensing performance and detection capabilities. The suggested geometric structure utilizes fused silica (Si) for its advantageous characteristics. The Sellmeier equation provided its refractive index (Akowuah et al. 2012),

$$n_{(Si)}^2(\lambda) = 1 + \sum_{i=1}^{i=3} \frac{M_i}{1 - \left(\frac{N_i}{\lambda}\right)^2} \tag{1}$$

We denote the effective refractive index of fused silica as $n_{Si}(\lambda)$, where λ represents the operating wavelength in μm. Equation 1 incorporates Sellmeier's constants with the following values: $M_1 = 0.696263$, $N_1 = 0.0684043$ μm, $M_2 = 0.4079426$, $N_2 = 0.1162414$ μm, $M_3 = 0.8974794$, and $N_3 = 9.896161$ μm. Temperature's impact on refractive index is negligible under conventional circumstances and therefore ignored (Tan 2021). The refractive index of fused silica varies with wavelength, the Sellmeier equation helps in determining
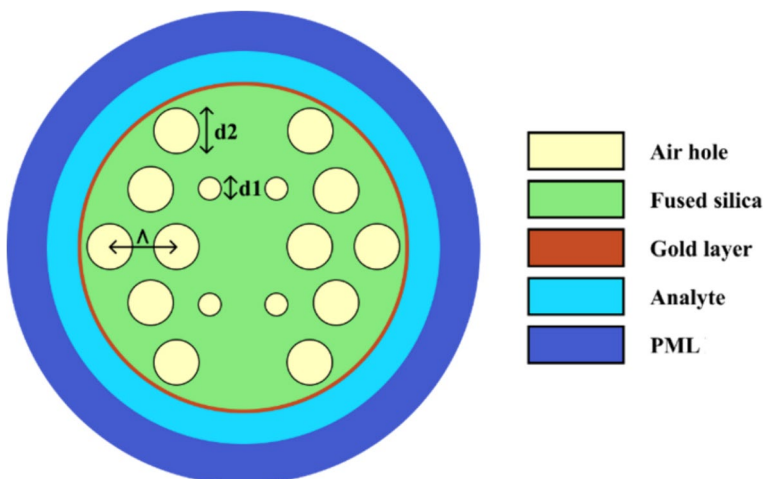

Fig. 1 The proposed sensor's cross-sectional view

this variable refractive index across the range of wavelengths used in the study. Light at various wavelengths travels through the PCF, generating a loss curve for both core and surface plasmon modes. By analyzing this curve, scientists can infer the refractive index of the analyte layer, ultimately identifying the material present.

Following the selection of gold as the plasmonic material, we deposit it on the sensor's external surface. The Drude-Lorentz formula plays a crucial role, yielding the gold film's dielectric constant and, through its inherent model, computing the dispersion as a function of wavelength (Vial et al. 2005),

$$\varepsilon_{Au}(\omega) = \varepsilon_\alpha - \frac{\omega_D^2}{\omega(\omega + i\gamma_D)} - \frac{\Delta_\epsilon \Omega_L^2}{(\omega^2 - \Omega_L^2) + i\Gamma_{L\omega}} \tag{2}$$

The Drude-Lorentz model incorporates parameters like plasma frequency (ωD), angular frequency (ω), damping coefficient (γD), weight factor ($\Delta\epsilon = 1.09$), Lorentz oscillator strength (ΩL), and spectral width (ΓL) with ε_α set at 5.9673. Specific values: $\frac{\omega L}{2\pi} = 2113.6$ THz, $\frac{\gamma D}{2\pi} = 15.92$ THz, $\frac{\Gamma_L}{2\pi} = 104.86$ THz and $\frac{\Omega_L}{2\pi} = 650.07$ THz.

A crucial parameter for designing biosensors is confinement loss which happens when the metal surface's plasmon mode and core mode pair at the phase-matching point. Unlike other types of fibers, photonic crystal fiber provides the valuable ability to control confinement loss through the number of air-hole rings. This design freedom allows us to achieve optimal levels of both confinement and loss for diverse applications (Selim Habib et al. 2012). Structures with more air-hole rings experience fewer losses. This loss, denoted as Lc, is obtained as –

$$L_c \left(\frac{dB}{cm} \right) = 8.686 \times k_0 I_m [n_{eff}] \times 10^4 \tag{3}$$

where $I_m[n_{eff}]$ is the imaginary part of the effective refractive index, k_0 is the wavenumber. It is possible to calculate the complex refractive index of the fundamental mode by using the Finite Element Method (FEM). This loss is contingent on various factors, with core size and pitch, as well as air-hole dimensions, being notable contributors. The quantity of rings in the cladding is also a crucial factor. This provides us with the possibility of obtaining a PCF with exceptionally low loss.

3 Results and discussion

The interaction of an electromagnetic wave with the metal field results in a collective oscillation of electrons at the metal–dielectric interface, creating a surface plasmon wave. The refractive index of an unknown analyte is significantly influenced by both the core-guided and surface plasmon polariton modes. During this research work, we exclusively emphasized the y-polarized fundamental core mode, as it exhibits a sharper and remarkable loss peak in this particular propagation direction. Figure 2, depicts the y-polarized core and SPP mode respectively, at an analyte RI of 1.38 with an operating wavelength of 0.78 μm.

In Fig. 3, the resonant frequency range as well as the fundamental modes (core guided and SPP) are illustrated for na = 1.38 in y-polarization. The dispersion relationship is investigated, taking into account the plasmonic material gold, with $t_g = 40$ nm. The green and blue lines represent the real parts of the effective indices (neff) for the fundamental core as well as SPP mode. At the resonated wavelength of 0.78 μm, there is
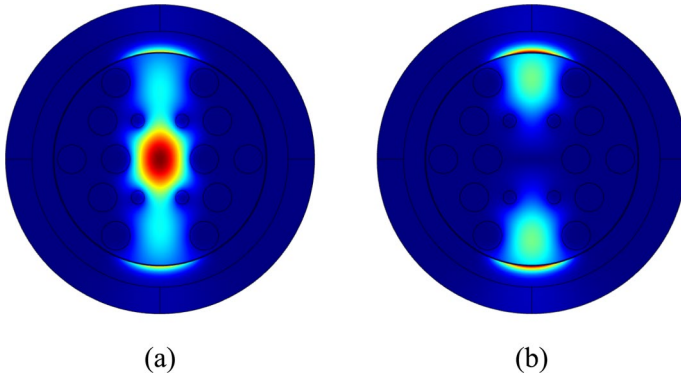
(a)   (b)

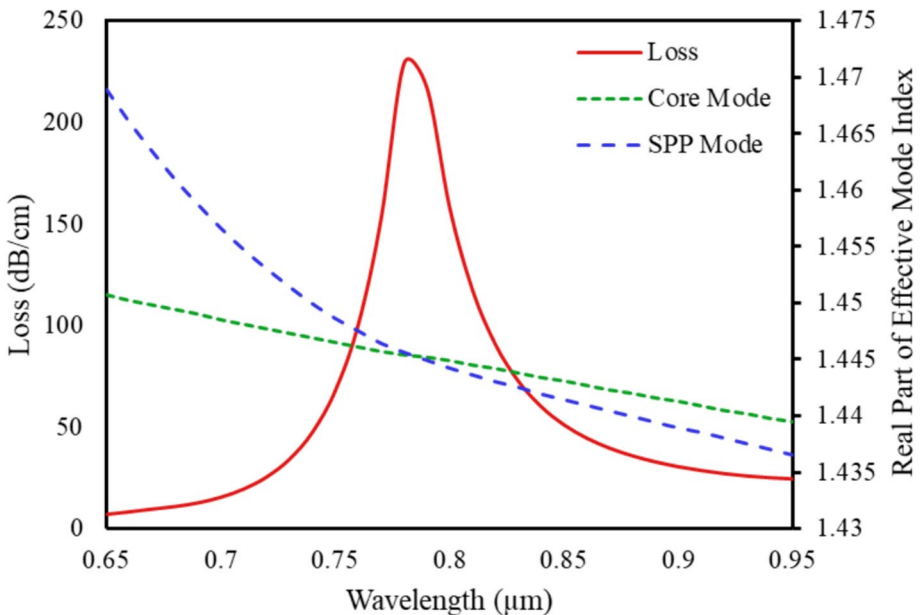**Fig. 2** Fundamental y-polarized **a** core and **b** SPP mode

Fig. 3 Relationship of dispersion among the spp and core-guided mode at analyte RI of 1.38

a match in the effective indices of the fundamental core (green) and SPP (blue) modes, resulting in a peak loss. This point is denoted as the resonance condition, where the plots intersect.

Analyte RI has the most significant effect on an SPR sensor's sensitivity. To evaluate the sensor's behaviors to dynamic variations in the refractive index, the sensor is tested using the optimized parameters. The refractive index order is diverse from 1.33 to 1.39 RIU. The phase alignment of the core and SPP mode ensures that the sensor is in a condition for maximum power transfer. Consequently, the sensor becomes sensitive to changes. With an increasing refractive index of the analyte, a rise in the spectrum of loss is observed. This indicates that the sensor can detect losses more accurately and hence is sensitive to that RI.

Consequently, with an increasing refractive index, the wavelength at which the largest loss is found moves to the right. Our analysis, as illustrated in Fig. 4 for y-polarizations, reveals that the maximum loss spectrum occurs at an analyte RI of 1.39. This configuration results in the highest sensitivity for both amplitude and wavelength interrogation.

Figure 4, illustrates the deviation in confinement loss with changes in refractive indices for a configuration featuring a 2 μm pitch, air hole diameters of 0.3 × Λ and 0.65 × Λ, and a 40 nm gold layer. The consistent loss is recorded at 56.471 dB/cm for an analyte refractive index of 1.33 at a wavelength of 690 nm. As the analyte refractive index increased incrementally from 1.33 to 1.39 (with an increase of 0.01), the peak loss's depth grew. A significant alteration in confinement loss is observed with the incremental rise in analyte RI, leading to a reduced index difference among the core and SPP modes. Additionally, the increase in analyte RI results in a right shift, changing the equivalent phase point at longer wavelengths.

The loss depths are sequentially measured at 69.471, 89.586, 117.1, 155.58, 229, and 385.6 dB/cm for refractive indices 1.34, 1.35, 1.36, 1.37, 1.38, and 1.39 respectively, at wavelengths 650, 670, 700, 730, 780 and 860 nm. The increased confinement is facilitated by higher loss depths, promoting greater field intrusion through the cladding region. Consequently, this directs increased energy transfer from the core mode to SPP mode, enhancing the analyte's interaction. Through careful experimental procedures, we determine the resonance wavelength shifts as 20, 20, 30, 30, 50, and 80 nm, corresponding to analyte RI increments of 0.01 across the range from 1.33 to 1.39, demonstrating a clear dependence between these optical properties.

For sensitivity calculations utilizing the wavelength interrogation method, the equation from Atakaramians (2011) is applied:
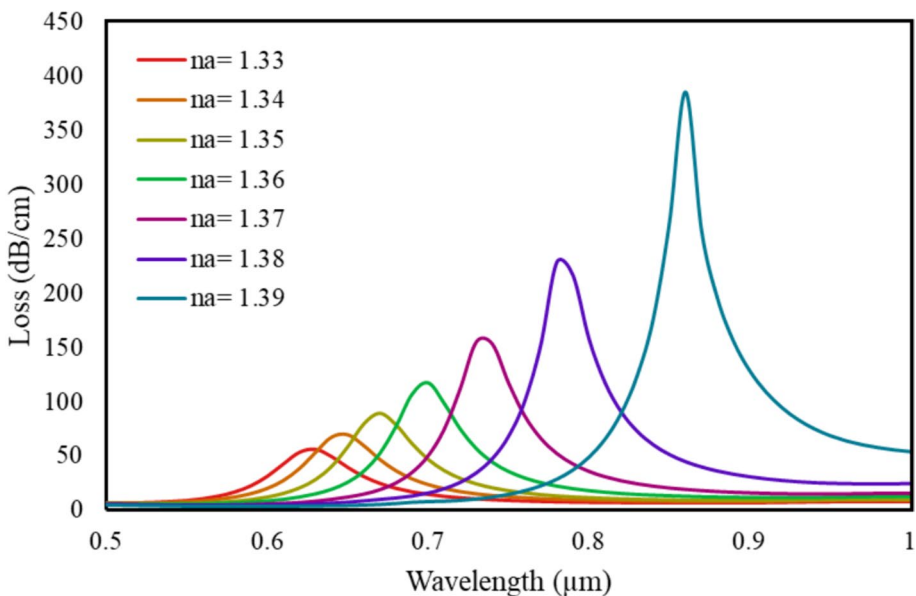

Fig. 4 Loss spectrum with RI variation

$$S_\lambda\left(\frac{nm}{RIU}\right) = \frac{\Delta\lambda_{peak}}{\Delta n_a} \tag{4}$$

In Eq. (4), $\Delta\lambda$peak and Δn_a stand for peak wavelength shift and analyte refractive index difference, respectively. The approximate wavelength sensitivities are determined as 2000, 2000, 3000, 3000, 5000, and 8000 nm/RIU at refractive indices 1.33, 1.34, 1.35, 1.36, 1.37 and 1.38, respectively.

Another critical parameter, sensor resolution, is computed by applying the equation from Guo et al. (2020):

$$R(RIU) = \Delta n_a \times \frac{\Delta\lambda_{min}}{\Delta\lambda_{peak}} \tag{5}$$

In Eq. (5), λ_{min} denotes the lowest spectral resolution. The wavelength resolutions are determined as 5×10^{-5}, 5×10^{-5}, 3.33×10^{-5}, 3.33×10^{-5}, 2×10^{-5}, and 1.25×10^{-5} RIU at refractive indices 1.33, 1.34, 1.35, 1.36, 1.37 and 1.38 respectively.

The wavelength interrogation approach only provides sensitivity at specific wavelengths. For this its application is expensive. On the other hand, unlike wavelength interrogation, amplitude sensitivity eliminates the need for interpolation, simplifying analysis and potentially reducing associated costs. The equation for amplitude sensitivity, sourced from Limpert et al. (2006), is expressed as:

$$S_A\left(RIU^{-1}\right) = -\frac{1}{\alpha\left(\lambda, n_a\right)}\frac{\partial a\left(\lambda, n_a\right)}{\partial n_a} \tag{6}$$

In Eq. (6), n_a denotes the analyte refractive index and $\alpha(\lambda, n_a)$ represents the confinement loss. Additionally, $\delta\alpha(\lambda, n_a)$ signifies the difference in confinement loss between two consecutive analyte refractive indices.

Figure 5, illustrates the amplitude sensitivity for optimal design, revealing values of 88.69, 118.002, 166.23, 248.85, 406.56, and 765.86 RIU^{-1} for analyte refractive indices of 1.33, 1.34, 1.35, 1.36, 1.37, and 1.38 respectively. The amplitude sensor resolutions achieved through the amplitude interrogation method are 1.13×10^{-4}, 8.47×10^{-5}, 6.02×10^{-5}, 4.02×10^{-5}, 2.46×10^{-5}, and 1.31×10^{-5} RIU.

Changing the gold layer's width visibly affects the loss's depth and amplitude sensitivity. In Fig. 6, it is observed that at an analyte refractive index (RI) of 1.35, the confinement losses exhibit values of 146.43, 89.586, and 47.038 dB/cm for corresponding gold layer depths of 30, 40, and 50 nm. At an analyte refractive index (RI) of 1.36, the confinement losses exhibit values of 226.9, 117.1, and 58.885 dB/cm for the same depths of the gold layer. As the gold layer thickness (t_g) increases, there is a decline in the loss indicating a relationship between loss and the rise of t_g. A shift is noticeable in the loss curve due to variations in the width of the gold coating.

In the initial stage of optimizing the reference structure, initial values for structural parameters are established, including a gold layer thickness (tg) of 40 nm, the diameter of the larger (d2) and smaller (d1) air holes are set at $0.60\times\Lambda$ and $0.30\times\Lambda$ respectively. To determine the optimum value, the pitch, $\Lambda = 1.9$, 2.0, and 2.1 μm is varied. In Fig. 7, the loss spectrum demonstrated depths of 106.49, 89.586, and 76.128 dB/cm for those pitch values respectively for an analyte refractive index of 1.35. For the analyte refractive index of 1.36, the loss spectrum demonstrated depths of 141.23, 117.1, and 98.807 dB/cm. The increase in pitch results in a higher effective refractive index
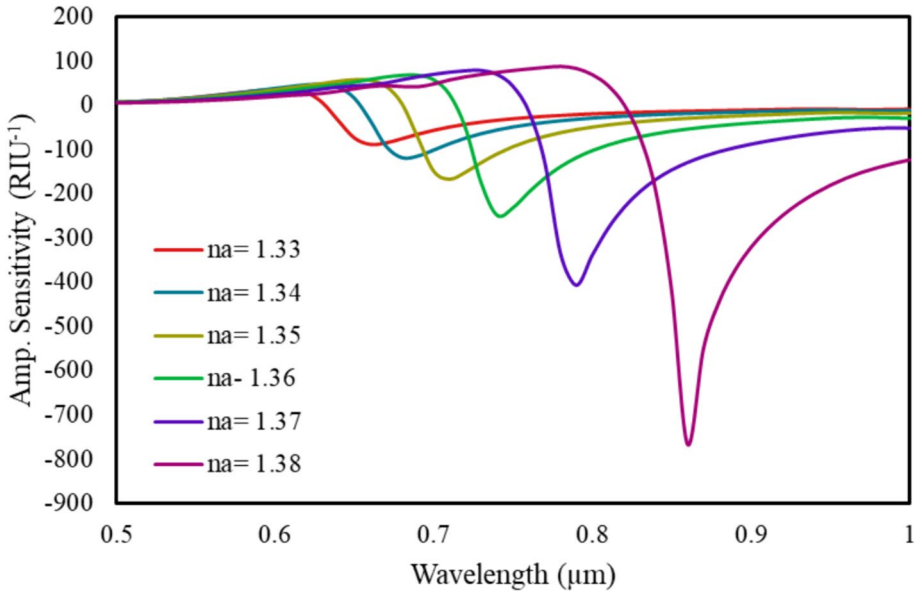
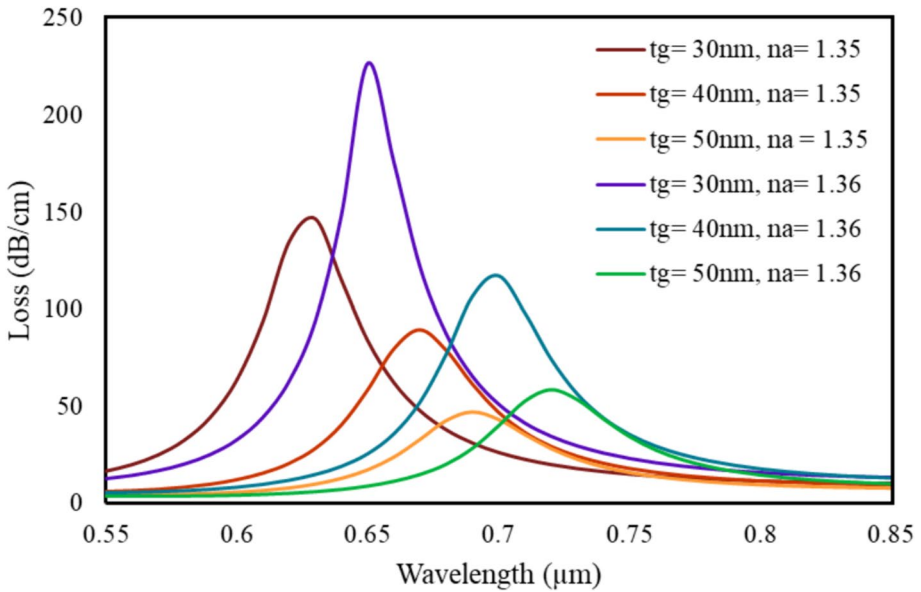**Fig. 5** Amplitude sensitivity with changes in refractive index

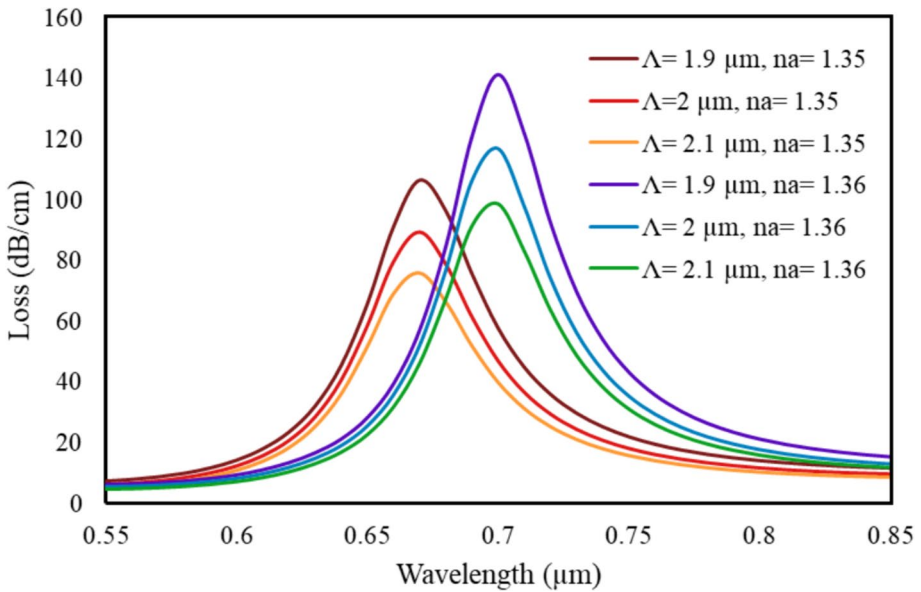**Fig. 6** The spectrum of losses with variations in gold layer thickness

Fig. 7 Loss spectrum with pitch variation

(RI) distinction among the core and cladding, consequently leading to a decrease in loss depth.

In the suggested sensor design, there are two categories of air holes: larger air holes characterized by a diameter of d2 and smaller air holes with a diameter of d1. Different combinations of diameters for the two sizes of air holes are explored to determine the most suitable diameter. Throughout the optimization process, the pitch ($\Lambda=2$ μm) and gold layer thickness (tg$=40$ nm) are maintained at constant values. As a general trend, it can be observed that enlarging the smaller air hole's diameter decreases confinement loss while increasing the diameter of the larger air hole leads to increased confinement loss. The reason for this is that reducing the smaller air hole's diameter attracts light toward the plasmonic layers, promoting increased interaction between light and material.
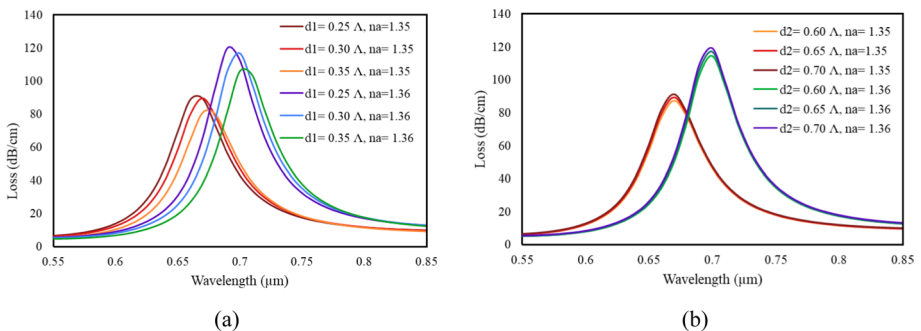

Fig. 8 Loss spectrum with variation in the diameter of **a** smaller and **b** larger air holes

In Fig. 8a, the impact of varying the diameter of smaller air holes (d1) on the loss curve is elucidated. The loss depths are recorded at 89.632, 89.586, and 81.112 dB/cm for air hole diameters of $0.25 \times \Lambda$, $0.3 \times \Lambda$, and $0.35 \times \Lambda$ correspondingly for analyte refractive index of 1.35. At a refractive index of 1.36, the loss depths are recorded at 120.07, 117.1, and 106.15 dB/cm for air hole diameters of $0.25 \times \Lambda$, $0.3 \times \Lambda$, and $0.35 \times \Lambda$ respectively. Notably, as the air hole diameter increased, the loss decreased.

Figure 8b provides an explanation of how the larger air hole's (d2) diameter changes affecting the loss curve. The loss depths are recorded at 87.638, 89.586, and 91.37 dB/cm for larger air hole diameters of $0.60 \times \Lambda$, $0.65 \times \Lambda$, and $0.70 \times \Lambda$, respectively for analyte refractive index of 1.35. At a refractive index of 1.36, the loss depths are recorded at 114.68, 117.1, and 119.26 dB/cm for larger air hole diameters of $0.60 \times \Lambda$, $0.65 \times \Lambda$, and $0.70 \times \Lambda$ respectively. Notably, the loss increased with the enlargement of the air hole diameter.

In Fig. 9, the relationship between resonated wavelength and analyte refractive index is depicted, with a linear fit applied at a 40 nm depth of the gold layer. The solid dotted line represents the linear fitting, and the square markers indicate the resonant wavelengths. The slope of the linear fit curve represents the average sensitivity. If the sensor exhibits linearity, predicting the resonant wavelength for higher analyte refractive indices becomes more straightforward. Greater linearity corresponds to a more proportional shift in the resonant wavelength. The correlation coefficient (R), which is obtained through linear regression, may serve as a representation of linearity. The linear fitting of the resonant wavelength is depicted in Fig. 9 as a function of the analyte refractive indices. The suggested sensor's linear fit regression equation is $y = -3.6071x - 4.1886$ and the Regression Coefficient is $R^2 = 0.9307$. The coefficient of determination (R^2) signifies the connection between resonant wavelength and analyte refractive index, and in Fig. 9, the linear fitting exhibits a
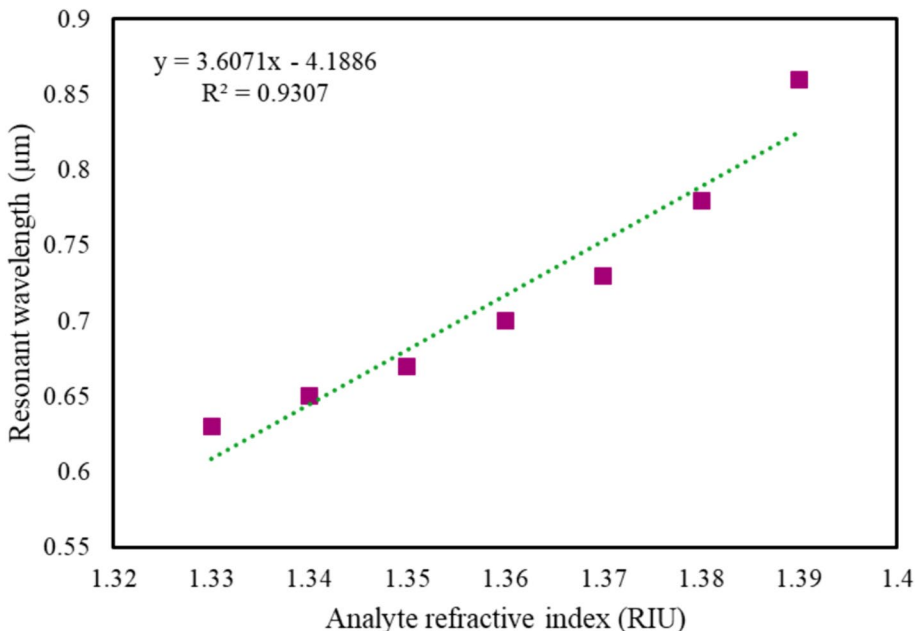

Fig. 9 Linear fitting in the y-polarized mode

Table 1 SPR sensor performance assessment with different analyte refractive indices

Analyte RI	Peak loss (dB/cm)	Resonance peak wavelength (µm)	Wavelength sensitivity (nm/RIU)	Wavelength resolution (RIU)	Amplitude sensitivity (RIU^{-1})	Amplitude resolution (RIU)
1.33	56.471	0.63	2000	5×10^{-5}	88.69	1.13×10^{-4}
1.34	69.471	0.65	2000	5×10^{-5}	118.002	8.47×10^{-5}
1.35	89.586	0.67	3000	3.33×10^{-5}	166.23	6.02×10^{-5}
1.36	117.1	0.70	3000	3.33×10^{-5}	248.85	4.02×10^{-5}
1.37	155.58	0.73	5000	2×10^{-5}	406.56	2.46×10^{-5}
1.38	229	0.78	8000	1.25×10^{-5}	765.86	1.31×10^{-5}
1.39	385.6	0.86	N/A	N/A	N/A	N/A

Table 2 A comparison of the suggested sensor with existing ones

References	Wavelength sensitivity (nm/RIU)	Wavelength resolution (RIU)	Amplitude sensitivity (RIU^{-1})	Amplitude resolution (RIU)
Rifat et al. 2017	4000	2.5×10^{-5}	478	2.1×10^{-5}
Chen et al. 2024	8000	1.5×10^{-5}	198.354	1.25×10^{-5}
Jabir and Areebi 2022	4000	2.5×10^{-5}	265	3.7×10^{-5}
Rifat et al. 2017	5723.5	1.74×10^{-6}	N/A	N/A
Sharmin 2018	2000	5×10^{-5}	140	7.1×10^{-5}
Seifouri et al. 2018	6000	1.67×10^{-5}	508	1.97×10^{-5}
Otupiri et al. 2015	4600	2×10^{-5}	425	2×10^{-5}
Proposed PCF-Based SPR Sensor	8000	1.25×10^{-5}	765.86	1.31×10^{-5}

desirable linearity. A linear relationship is advantageous for average sensitivity and resolution as it simplifies the identification mechanism. The proposed design can be feasibly manufactured utilizing techniques such as chemical vapor deposition (CVD) or atomic layer deposition (ALD), both of which are effective in applying an even gold coating on curved surfaces (Rifatet. 2015).

Table 1, presents the obtained parameters from our sensor's analysis for the analyte refractive index in the y-polarization range of 1.33–1.39. Maximal AS of 765.86 RIU^{-1} and maximal WS of 8000 nm/RIU are found at RI = 1.38.

The recently published PCF sensors are contrasted with the proposed sensor's performance. Table 2, provides a succinct overview of various surface plasmon resonance (SPR) sensors, delineating their respective capabilities in terms of wavelength and amplitude sensitivity as well as resolution. Notable sensors include those with high wavelength sensitivity, such as Reference (Chen et al. 2024) with 8000 nm/RIU, and those exhibiting remarkable amplitude sensitivity, exemplified by Seifouri et al. (2018) at 508 RIU^{-1}. The proposed PCF-based SPR sensor stands out with an impressive wavelength sensitivity of 8000 nm/RIU, a low resolution of 1.25×10^{-5} RIU, and a substantial amplitude sensitivity of 765.86 RIU^{-1}. This comparison underscores the advancements in SPR sensor technology, emphasizing the perspective of the proposed PCF-based sensor for high-sensitivity applications.

4 Conclusion

In this study, a novel modified hexagonal photonic crystal fiber (PCF) based surface plasmon resonance (SPR) sensor is introduced that boasts heightened sensitivity and improved resolution. The gold is the preferred plasmonic material and it is carefully placed next to the analyte layer on the PCF's exterior. This deliberate arrangement aims to streamline the fabrication process and enhance practical sensing capabilities. The research delves into various performance parameters, revealing that the suggested sensor achieves a maximum wavelength sensitivity of 8,000 nm/RIU and an amplitude sensitivity of 765.86 RIU^{-1} with the optimized parameters of the sensor. Notably, the sensor demonstrates a dynamic detection range, responding effectively to refractive index values within the range of 1.33 to 1.39. This PCF-based SPR sensor demonstrates a remarkable resolution of 1.25×10^{-5} for wavelength sensitivity and 1.31×10^{-5} for amplitude sensitivity, positioning it as a highly precise biosensor for the detection of biological and biochemical samples. In addition, the suggested sensor has impressive linear characteristics, combining outstanding sensing abilities, appropriate linearity, and practical simplicity.

Declarations

Conflict of interest The authors declare no competing interests.

References

Akowuah, E.K., Gorman, T., Ademgil, H., Haxha, S., Robinson, G.K., Oliver, J.V.: Numerical analysis of a photonic crystal fiber for biosensing applications. IEEE J. Quantum Electron **48**(11), 1403–1410 (2012)

An, S., Li, H. Wang., Zhang, X.: Metal oxide-graphene-based quasi-D-shaped optical fiber plasmonic biosensor. IEEE Photonics J. **9**(4), 1–9 (2017)

Atakaramians, S.: Terahertz waveguides: a study of microwires and porous fibres. Ph.D. dissertation, Faculty of Engineering, University of Adelaide, Australia, (2011)

Chen, R., Patel, S., Wang, L., et al.: External metal-coated sensors for enhanced sensitivity and simplified manufacture. Opt. Lett. **49**(11), 2957–2960 (2024)

Gangwar, R.K., Singh, V.K.: Highly sensitive surface plasmon resonance based D-shaped photonic crystal fiber refractive index sensor. Plasmonics **12**(5), 1367–1372 (2017)

Guo, Z., Fan, Z., Kong, X., Meng, Z.: Photonic crystal fiber based wide-range of refractive index sensor with phase matching between core mode and metal defect mode. Opt. Commun. **461**, 125233 (2020)

Hasan, M.R., Akter, Sanjida, Rifat, Ahmmed A., Rana, Sohel, Ahmed, Kawsar, Ahmed, Rajib, Subbaraman, Harish, Abbott, Derek: Spiral photonic crystal fiber-based dual-polarized surface plasmon resonance biosensor. IEEE Sensors J. **18**(1), 133–140 (2018). https://doi.org/10.1109/JSEN.2017.2769720

Hossain, M.B., et al.: Numerical analysis and design of photonic crystal fiber-based surface plasmon resonance biosensor. J. Sensor Technol. **9**, 27–34 (2019)

Jabir, J.N., Areebi, N.A.: High sensitively of double-core surface plasmon resonance biosensor based on photonic crystal fiber. Opt. Quant. Electron. **54**, 626 (2022). https://doi.org/10.1007/s11082-022-03950-y

Jing, J., Liu, K., Jiang, J., Xu, T., Wang, S., Ma, J., Zhang, Z., Zhang, W., Liu, T.: Performance improvement approaches for optical fiber SPR sensors and their sensing applications. Photon. Res. **10**, 126–147 (2022)

Limpert, J., et al.: Extended single-mode photonic crystal fiber lasers. Optic Express **14**(7), 2715–2720 (2006)

Liu, Y., Zhang, J., Wang, H., et al.: Experimental study of dual-parameter SPR sensor with integrated sensing channel. IEEE Sens. J. **23**(8), 8385–8390 (2023)

Miyazaki, Celina M., Shimizu, Flávio. M., Ferreira, Marystela: Surface plasmon resonance (SPR) for sensors and biosensors. In: Nanocharacterization Techniques, pp. 183–200. Elsevier (2017). https://doi.org/10.1016/B978-0-323-49778-7.00006-0

Momota, M.R., Hasan, M.R.: Hollow-core silver coated photonic crystal fiber plasmonic sensor. Opt. Mater. **76**, 287–294 (2018)

Ng, W., Aoni, RifatAhmmed, Wong, W.R., Mahdiraji, GhafourAmouzad&Adikan, Faisal.: A Novel diamond ring fiber-based surface plasmon resonance sensor. Plasmonics **13**, 1–6 (2018). https://doi.org/10.1007/s11468-017-0617-y

Otupiri, R., Akowuah, E.K., Haxha, S.: Multi-channel SPR biosensor based on PCF for multi-analyte sensing applications. Opt. Express **23**(12), 15716 (2015). https://doi.org/10.1364/OE.23.015716

Rifat, A., Hasan, M.R., Ahmed, R., Butt, H.: Photonic crystal fiber-based plasmonic biosensor with external sensing approach. J. Nanophotonics **12**(1), 012503 (2017)

Rifat, A.A., Mahdiraji, G.A., Ahmed, R., Chow, D.M., Sua, Y.M., Shee, Y.G., MahamdAdikan, F.R.: Copper-graphene-based photonic crystal fiber plasmonic biosensor. IEEE Photonics J. **7**(1), 1–8 (2016)

Rifat, A., et al.: Surface plasmon resonance photonic crystal fiber biosensor: a practical sensing approach. IEEE Photonics Technol. Lett. **27**(15), 1628–1631 (2015)

Rifat, Ahmmed A., Ahmed, Rajib, Yetisen, Ali K., Butt, Haider, Aydin Sabouri, G., Mahdiraji, Amouzad, Yun, Seok Hyun, MahamdAdikan, F.R.: Photonic crystal fiber based plasmonic sensors. Sensors Actuators B: Chem. **243**, 311–325 (2017). https://doi.org/10.1016/j.snb.2016.11.113

Seifouri, M., Rouini, M.A., Olyaee, S.: Design of a surface plasmon resonance biosensor based on photonic crystal fiber with elliptical holes. Opt. Rev. **9**, 27–34 (2018)

Selim Habib, Md., Samiul Habib, Md., Razzak, S.M.A.: Study on dual-concentric-core dispersion compensating photonic crystal fiber. Int. J. Eng. Technol **1**(4), 377–383 (2012)

Sharmin, S., Bosu, A., Akter, S.: Gold-Coated Photonic Crystal Fiber-Based Plasmonic Biosensor. Int. Conf. Adv. Electr. Electron Eng. Gazip, Bangladesh, (2018). https://doi.org/10.1109/ICAEEE.2018.8643003

Smith, A., Johnson, B., Lee, C., et al.: Modulation of the sensing bandwidth of dual-channel SPR sensors by TiO2 film. Opt. Laser Technol. **169**, 110105 (2024)

Tan, C.Z.: Dependence of the refractive index on density, temperature, and the wavelength of the incident light. Eur. Phys. J. B (2021). https://doi.org/10.1140/epjb/s10051-021-00147-2

Vial, A., Grimault, A.-S., Mac´ias, D., Barchiesi, D., De La Chapelle, M.L.: Improved analytical fit of gold dispersion: Application to the modeling of extinction spectra with a finite-difference time-domain method. Physical Review B **71**(8), 085416 (2005)